remote sensing

MDPI

Article

UAV RGB Imagery as an Early-Warning Tool of Wheat Rust Pathogen-Induced Physiological Changes

Moussa El Jarroudi [1], Louis Kouadio [2,3,*], Jonathan Peereman [1] and Marco Beyer [4]

[1] SPHERES Research Unit, Department of Environmental Sciences and Management, University of Liège, 6700 Arlon, Belgium; meljarroudi@uliege.be (M.E.J.); jonathan.peereman@uliege.be (J.P.)
[2] Africa Rice Center (AfricaRice), Bouake 01, Côte d'Ivoire
[3] Centre for Applied Climate Sciences, Institute for Agriculture, Climate and the Environment, University of Southern Queensland, Toowoomba, QLD 4350, Australia
[4] Luxembourg Institute of Science and Technology, 41 Rue du Brill, L-4422 Belvaux, Luxembourg; marco.beyer@list.lu
* Correspondence: a.kouadio2@cgiar.org

Highlights

What are the main findings?

- Unmanned Aerial Vehicle (UAV)-based red–green–blue (RGB) imagery uncovers a previously unquantified pre-symptomatic phase of wheat stripe and leaf rust epidemics.
- The pre-symptomatic phase was characterized by early changes in green–red spectral dynamics.
- Flattening of RGB spectral slopes was a robust early-warning indicator of pathogen-induced physiological stress.

What are the implications of the main findings?

- RGB UAV imagery can help detect wheat stripe rust and leaf rust early, making it useful for both diagnosis and early-warning monitoring.
- This framework supports targeted disease management decisions, with implications for precision agriculture, optimization of fungicide application, and scalable crop health monitoring.

Abstract

Remote sensing of crop diseases has traditionally focused on detecting visible symptoms, often limiting intervention to advanced stages of epidemic development. This study investigates whether high-resolution unmanned aerial vehicles (UAV)-based red–green–blue (RGB) imagery can reveal earlier physiological destabilization preceding visible symptoms of wheat stripe rust and wheat leaf rust. UAV imagery was acquired at four winter wheat-growing sites in Luxembourg during the 2018/2019 season. Temporal dynamics of green–red spectral slopes were analyzed and compared with ground-based disease severity observations to identify potential pre-symptomatic spectral signals. A consistent flattening of the green–red spectral slope was detected prior to a rapid increase in visually assessed severity for both diseases. However, the length of this pre-symptomatic window varied between the two diseases: it lasted 7 to 14 days for wheat stripe rust and 5 to 10 days for wheat leaf rust. Likewise, the reduction in spectral slope magnitude was slightly greater for wheat stripe rust (65–80%) than for wheat leaf rust (60–75%), indicating that the temporal lead time and intensity of the spectral response were disease-dependent. During the pre-symptomatic phase, the spectral dynamics reflected latent physiological changes rather than visible disease severity. Strong correlations emerged only after the epidemic transition. These findings demonstrate that UAV-based RGB imagery could capture a

Check for updates

Academic Editors: Huajian Liu and Haiguang Wang

Received: 21 April 2026
Revised: 26 May 2026
Accepted: 28 May 2026
Published: 1 June 2026

Copyright: © 2026 by the authors. Licensee MDPI, Basel, Switzerland. This article is an open access article distributed under the terms and conditions of the Creative Commons Attribution (CC BY) license.

distinct pre-symptomatic phase of stripe rust and leaf rust epidemics in winter wheat. Interpreting RGB spectral dynamics as early-warning indicators rather than merely as static severity proxies can guide proactive disease monitoring and precision agriculture.

Keywords: spectral dynamics; plant disease monitoring; stripe rust; leaf rust; disease management

1. Introduction

Plant diseases remain one of the major threats to global food security, with fungal pathogens alone accounting for yield losses exceeding 15–20% in major cereal crops worldwide [1,2]. Among them, wheat rust diseases—particularly stripe rust (WSR, caused by *Puccinia striiformis* f. sp. *tritici*) and leaf rust (WLR, caused by *Puccinia triticina*)—are responsible for recurrent epidemics with severe agronomic and economic impacts across temperate regions [3,4]. Remote sensing has become a cornerstone of modern crop disease surveillance, offering non-destructive, spatially explicit information on crop health across scales ranging from leaf to landscape [5–8]. Most operational approaches, however, remain fundamentally symptom-oriented: they aim to discriminate healthy from diseased vegetation once visual or biochemical alterations have already emerged [9,10]. Early detection of shifts in crop–pathogen dynamics would enable more proactive disease monitoring, timelier intervention, and reduced yield losses. However, most current remote sensing frameworks are primarily designed to map established disease patterns in space—answering the question "where is the disease?"—rather than detecting the earlier transition toward epidemic development. This limitation partly reflects both conceptual and operational constraints. Conceptually, many approaches focus on severity estimation once symptoms are visible, rather than on identifying early functional changes in the crop pathosystem preceding symptom expression. Operationally, high-resolution multispectral and hyperspectral imaging systems, while powerful for disease characterization, remain costly and logistically demanding to deploy at high temporal frequency across large agricultural landscapes. As a result, the strategic question shifts from "when does the crop pathosystem become unstable?" to a more mechanistically and ecologically grounded formulation: "when does the crop pathosystem cross a critical threshold beyond which epidemic amplification becomes inevitable?"; that is, when do early signal changes translate into a self-sustaining epidemic trajectory?

Hyperspectral and multispectral data have demonstrated strong capabilities for disease detection [6–8]. Recent advances in unmanned aerial vehicle (UAV) platforms have renewed interest in red–green–blue (RGB) imagery as a low-cost, high-resolution alternative for crop monitoring. Despite its limited spectral dimensionality, UAV-based RGB imagery acquired from low-altitude UAV platforms can nonetheless help detect subtle variations in crop canopy characteristics under operational field conditions. Previous work has demonstrated that UAV-based RGB imagery can successfully quantify canopy cover, biomass, and disease severity in several crop systems [7,11]. RGB-derived indices exploiting visible reflectance dynamics have proven effective for quantifying WSR and WLR severities across key phenological stages. For example, the WSR index, based on additive combinations of the digital numbers of the red and green channels, and the WLR index, derived from RGB color transformations targeting brown lesion signatures, have demonstrated strong agreement between disease estimates derived from UAV imagery and ground observations [7]. In a broader context, vegetation indices derived from RGB imagery, such as the excess green index (ExG) [12] and color index of vegetation extraction (CIVE) [13],

have effectively detected canopy discoloration and structural changes caused by disease in real-world settings [14]. This demonstrates the valuable role of RGB imagery for accurately quantifying plant disease in precision agriculture [8]. However, most existing studies have treated UAV-based RGB imagery as a diagnostic tool for detecting disease symptoms only after they become visually apparent [7,8,15]. This symptom-centric paradigm has proven effective for mapping disease severity and spatial patterns in fields, yet it largely overlooks the possibility that RGB spectral dynamics may contain earlier signals of physiological disruption preceding visible symptom expression. Such pre-symptomatic changes, potentially linked to chlorophyll degradation, altered pigment composition, or canopy structural adjustments, remain insufficiently explored in RGB-based disease monitoring frameworks [5,16].

From a systems perspective, plant disease epidemics are not merely accumulations of lesions but emergent phenomena arising from nonlinear interactions between host physiology, pathogen development, and microclimatic forcing [17,18]. Increasing evidence from ecology and climate science indicates that complex biological systems often exhibit early-warning signals prior to abrupt regime shifts or functional collapse. These signals include rising temporal variance, increasing autocorrelation, and systematic changes in recovery dynamics, as well as directional trends in key state variables and their rates of change over time [19–21]. In remote sensing applications, such directional trends can be quantified as temporal slopes of spectral indicators—defined as the rate of change in vegetation-related reflectance metrics (e.g., greenness, canopy structure, or color-based indices) over successive observations. They provide a measurable proxy for progressive physiological disruption prior to the onset of visible symptoms [19,21].

In crop pathosystems, these early destabilization phases are rarely observed directly, as physiological stress often precedes visible symptoms by days or weeks [22]. Yet, subtle alterations in pigment dynamics, energy balance, and canopy structure may already be encoded in the optical signal, particularly within the visible spectrum where chlorophyll absorption dominates [23,24]. Early symptoms of WSR typically appear as small chlorotic flecks or narrow yellow streaks aligned with the leaf veins, generally affecting approximately 1 to 5% of the leaf area before visible sporulation develops. As the epidemic progresses, these lesions evolve into characteristic linear rows of yellow-orange uredinia that may coalesce, frequently reaching 20 to 60% of the leaf area under conducive conditions and leading to extensive chlorosis and premature senescence. In contrast, early symptoms of WLR typically appear as small, scattered chlorotic flecks affecting approximately 1 to 3% of the leaf area, which later develop into discrete, round to oval orange-brown uredinia distributed irregularly across the leaf surface. Under severe infection, WLR severity could reach approximately 15 to 40% of the leaf area. Both diseases can ultimately induce widespread tissue necrosis, canopy discoloration, and accelerated canopy collapse, with notable consequences for photosynthetic function and yield [4,25–27]. These well-characterized visual trajectories motivate a fundamental and largely untested hypothesis: that RGB spectral dynamics may capture an earlier, pre-symptomatic destabilization phase of crop disease epidemics, reflecting progressive physiological disruption before symptoms become visually apparent.

To address this question, we propose a conceptual and analytical shift in the use of UAV RGB imagery—from disease detection to early-warning sensing of physiological instability. Using high-resolution UAV RGB images acquired over wheat fields affected by WSR and WLR, we hypothesize that pathogen infection induces a systematic flattening of the green–red spectral slope, reflecting a progressive decline in chlorophyll functionality and metabolic coherence prior to the onset of severe symptoms. Rather than treating RGB indices as static severity estimators, we interpret their temporal evolution as state variables of the crop pathosystem. Within this framework, changes in the green–red spectral

slope function as spectral early-warning signals (SEWS), indicating the onset of a critical transition from physiological stability to epidemic outbreak.

This study aimed at (1) reinterpreting UAV-based RGB spectral dynamics as indicators of physiological destabilization rather than mere disease symptom expression; (2) identifying pre-symptomatic spectral signatures associated with WSR and WLR epidemics in winter wheat; (3) quantifying the temporal lead time between spectral destabilization and visible disease severity; and (4) establishing a conceptual early-warning framework linking UAV RGB imagery, plant physiology, and epidemic dynamics. By reframing low-cost RGB imagery as a high-frequency early-warning sensor, this work opens new perspectives for anticipatory disease management, decision support systems, and large-scale crop health surveillance.

2. Conceptual Framework

2.1. RGB Spectral Slopes as State Variables of Canopy Physiological Status

Despite their limited spectral resolution, RGB sensors capture canopy responses driven primarily by pigment dynamics, leaf structure, and illumination geometry [11,28,29]. Within the visible spectrum, chlorophyll absorption dominates reflectance patterns, particularly along the green–red axis [23]. Under healthy conditions, wheat canopies exhibit a pronounced negative slope between green and red reflectance, reflecting high chlorophyll efficiency and physiological coherence. As stress develops—whether due to senescence or pathogen infection—chlorophyll absorption in the red band decreases, resulting in a progressive flattening of this slope [10]. In this framework, the green–red spectral slope is interpreted not as a symptom-based index, but as a state variable reflecting the functional integrity of the crop canopy. Temporal changes in this slope therefore provide insight into system stability, rather than merely quantifying disease severity.

2.2. Definition of Spectral Early-Warning Signals

The concept of early-warning signals has been widely applied in ecology and climate science to anticipate critical transitions, where systems exhibit detectable changes in variance, temporal slopes, or autocorrelation prior to abrupt regime shifts [19–21]. These signals emerge from the progressive erosion of system resilience under increasing external stressors, ultimately leading to nonlinear responses near tipping points. Transposing this theoretical framework to crop pathosystems, we define spectral early-warning signals (SEWS) as systematic, time-dependent alterations in canopy spectral dynamics that precede rapid increases in visually assessed disease severity. In this context, the green–red spectral slope is conceptualized as a primary state variable, representing the normalized contrast between green and red canopy reflectance and serving as a proxy for canopy physiological integrity. Its progressive flattening over time would reflect a decline in chlorophyll efficiency and metabolic coherence at the canopy level, thereby indicating a loss of physiological stability.

Beyond this baseline indicator, the rate of spectral slope change, defined as the first-order temporal derivative of the green–red slope, provides a dynamic measure of system destabilization. An accelerated decline in this rate is hypothesized to precede the appearance of visible symptoms, reflecting rapid physiological perturbations induced by pathogen pressure. This transition culminates in a spectral destabilization point, defined as the stage at which the rate of the green–red spectral decline exceeds baseline variability, indicating a threshold-like shift and signaling a critical loss of canopy resilience. Importantly, it defines the onset of a pre-symptomatic window, corresponding to the time interval between changes in spectral signals and the subsequent epidemic acceleration phase. This lead time, expected to vary across sites and diseases, reflects latent physiological stress not yet

expressed as visible lesions and therefore provides a quantitative measure of anticipatory detection capacity.

The independence of SEWS from conventional disease assessments is evaluated through the spectral–severity decoupling index, defined as the correlation between the spectral slope and visually assessed disease severity during early epidemic stages. A weak correlation during this phase supports the hypothesis that spectral signals capture early physiological stress before symptom expression, thereby validating SEWS as robust and independent early-warning indicator. In this study, a pronounced reduction in the magnitude of the green–red spectral slope, combined with an acceleration in its temporal decline, is hypothesized to signal the approach of an epidemic transition, consistent with nonlinear system behavior near critical thresholds [30].

2.3. Hypotheses and Testable Predictions

Based on the SEWS framework and prior knowledge of WSR and WLR epidemiology and plant physiological responses, the following hypotheses were tested:

H1: *WSR and WLR infection induce measurable destabilization of RGB spectral dynamics before pronounced increases in visible disease severity.*

H2: *A marked change in the green–red spectral slope precedes epidemic acceleration with a measurable temporal lead, thereby delineating a pre-symptomatic destabilization window.*

H3: *During the pre-symptomatic phase, spectral dynamics are not expected to correlate with disease severity assessed at the same time point, as visible symptoms are absent. Instead, these early spectral fluctuations reflect latent physiological perturbations that precede symptom expression, and their association with disease severity becomes significant only after the epidemic onset.*

These hypotheses were evaluated using UAV-based RGB time series combined with ground-based disease assessments previously reported [7].

2.4. Conceptual Illustration of SEWS

Three successive phases are conceptualized along the epidemic timeline within the SEWS framework (Figure 1). These stages comprise: (i) a stable phase, characterized by a high spectral slope magnitude and low apparent disease severity; (ii) a pre-symptomatic transition phase, during which progressive changes in the green–red spectral slope indicate emerging physiological perturbations while visible disease severity remains low; and (iii) an epidemic expansion phase, marked by a rapid increase in disease severity following earlier spectral alterations. The temporal decoupling between spectral alterations and the escalation of visible symptoms defines a potential early-warning window (i.e., lead time) that can be leveraged for anticipatory disease management. From this perspective, affordable, high-resolution UAV RGB imagery serves not only as a diagnostic tool but also as a sensing system capable of detecting subtle early signs of instability in crop systems before visible disease symptoms emerge.

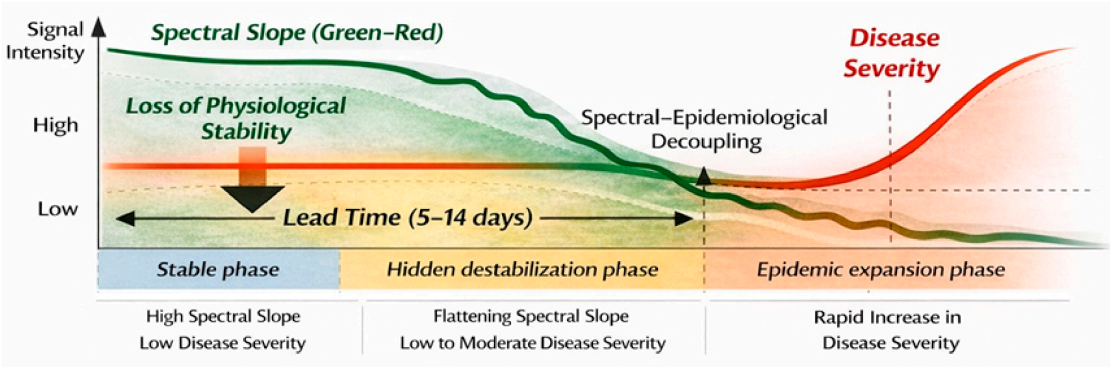


Figure 1. Conceptual framework of the spectral early-warning signals (SEWS) for wheat rust epidemics: temporal decoupling between canopy physiological dynamics and disease development during wheat rust epidemics. The green curve represents the temporal evolution of the green–red spectral slope derived from unmanned aerial vehicle-based Red–Green–Blue imagery, whereas the red curve represents disease severity assessed through conventional visual scoring. The pre-symptomatic destabilization phase is characterized by a progressive decline in spectral stability while disease symptoms remain largely undetectable. This phase defines a critical early-warning window during which spectral indicators anticipate epidemic onset before visible symptom expression. The transition point marks a spectral–epidemiological coupling associated with the onset of rapid disease expansion. This illustration was generated using ChatGPT based on GPT-5.3. It is a conceptual representation designed to reflect biologically realistic disease progression patterns rather than specific field observations.

3. Materials and Methods

3.1. Study Sites, Experimental Design and Disease Monitoring

This study used high-resolution UAV RGB datasets acquired in commercial winter wheat (*Triticum aestivum* L.) fields at four experimental sites (Bettendorf, Bicherhaff, Koerich, and Weiswampach) in the Grand Duchy of Luxembourg (GDL) during the 2018/2019 growing season (Figure 2). The experimental sites encompassed a range of pedoclimatic conditions, cultivars, and fungicide treatments, ensuring variability in disease pressure and canopy development. These sites were selected within the framework of a large-scale in-season disease monitoring program conducted in the GDL since 2004 [7,31]. Wheat was generally sown around mid-October across most sites, except at Bettendorf, where sowing occurred during the last week of October (Table S1). Crop management practices, including sowing and harvesting methods, fertilization, and weed control, were representative of standard wheat production systems in the GDL [7,31].

The experiment followed a completely randomized block design with four replicates, each replicate plot covering 12 m^2. Each randomized block included both fungicide-treated and non-treated (control) plots. The growth stage (GS) was assessed according to the Zadoks' decimal code [32]. The fungicides used were commercially available products; they were applied according to manufacturers' and official recommendations. All plots received 40–70 kg N ha^{-1} as ammonium nitrate at GS25, followed by 60–70 kg N ha^{-1} at GS32 and a final application of 65–95 kg N ha^{-1} at GS59. Fungicide treatments comprised control plots (no fungicide applied), T1 plots receiving a single fungicide application, T3a plots receiving three applications with the last spray applied at GS59, and T3b plots receiving three applications with the last spray applied at GS69.

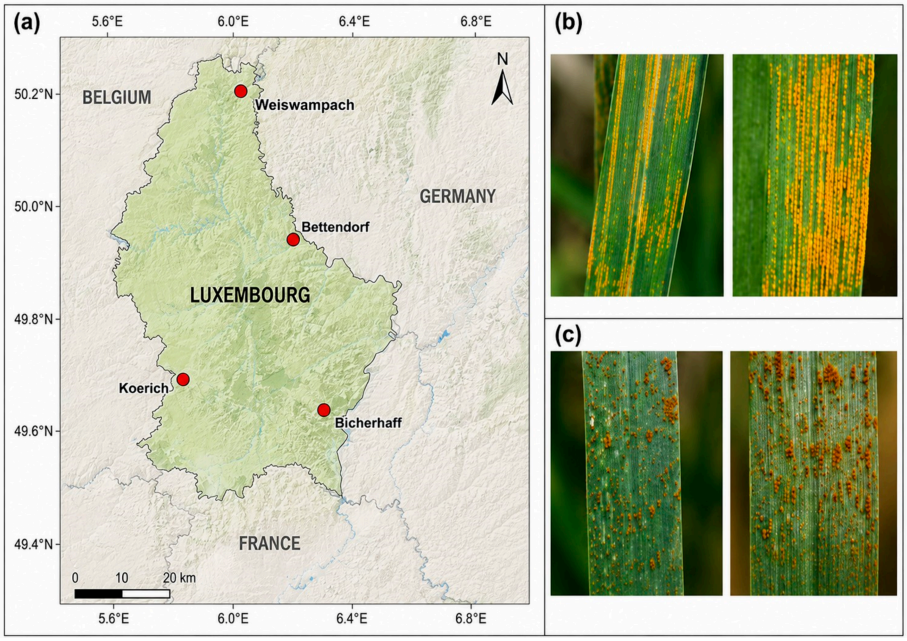


Figure 2. (**a**) Geographical location of the four study sites in the Grand Duchy of Luxembourg. (**b**) Photos of wheat leaves infected by stripe rust (caused by *Puccinia striiformis* f. sp. *tritici*). (**c**) Photos of wheat leaves infected by leaf rust (caused by *P. triticina*). Both diseases resulted from natural infection.

WSR and WLR epidemics were monitored weekly from April to July 2019 at each site. For each plot, ten plants were randomly selected at the beginning of the monitoring season and assessed repeatedly throughout the season following standardized protocols. All the diseases resulted from natural infection. Disease severity was assessed visually as the percentage of diseased leaf area on the selected plants. Visual assessments were conducted by four raters: two plant pathologists with extensive experience in disease assessment and two agronomists also experienced in wheat disease assessment. To maintain consistency, the same rater assessed each replicate throughout the monitoring period. Stripe rust and leaf rust were recorded separately at each observation date to preserve disease-specific epidemic dynamics and avoid conflating the two pathosystems. These ground-based observations served as independent reference data for evaluating spectral dynamics and epidemic progression. Potential sources of uncertainty in visual disease severity assessments included observer subjectivity, spatial heterogeneity of symptoms within plots, partial occlusion of lower leaves by the upper canopy, and variability in lesion visibility between early and advanced stages of the epidemic. Note that no molecular analyses for rust identification were carried out. Consequently, disease diagnosis relied on expert visual identification under field conditions.

3.2. UAV RGB Image Acquisition, Preprocessing, and Disease Severity Estimates

RGB imagery was acquired using a UAV-mounted RGB camera onboard a DJI Phantom 4 Pro platform (DJI, Shenzhen, China). UAV flights were conducted on four key dates between May and July 2019, corresponding to the main phases of canopy development and rust epidemic progression (24 May, 5 June, 19 June, and 3 July 2019) (Table 1). Flights were performed between approximately 11:00 and 16:00 local time under stable weather conditions and, whenever possible, under homogeneous sky illumination to minimize variability associated with solar angle, cloud cover, and changing light intensity. Flights were conducted at low altitude (approximately 10 m above ground level) in nadir view to reduce bidirectional reflectance effects and maintain consistent canopy observation geometry. The airspeed was set at 4 m s^{-1}, with 85% front and 75% side image overlaps,

resulting in a ground sampling distance of 0.28 cm. Flight missions were planned using the Pix4D capture software (Pix4D S.A., Lausanne, Switzerland).

Table 1. Overview of unmanned aerial vehicle (UAV) data acquisition at the study sites in 2019 in the Grand Duchy of Luxembourg [7].

Date	Site	Local Times (Start–End) at UAV Flight	Crop Growth Stage (GS)	Illumination Condition
15 May	Bettendorf	12:05–12:37	GS37	Sunny
	Bicherhaff [1]	13:15–13:30	GS37	
	Koerich	14:17–14:35	GS32	
	Weiswampach	15:11–15:28	GS32	
24 May	Bettendorf	11:14–11:40	GS42	Sunny
	Bicherhaff	12:30–12:44	GS39	
	Koerich	13:22–13:36	GS37	
	Weiswampach	14:02–14:15	GS39	
5 June	Bettendorf	12:15–12:48	GS57	Cloudy
	Bicherhaff	13:35–13:53	GS55	
	Koerich	14:33–14:53	GS52	
	Weiswampach	15:40–15:57	GS45	
3 July	Bettendorf	12:07–12:41	GS82	Sunny
	Bicherhaff	13:22–13:40	GS80	
	Koerich	14:21–14:44	GS77	
	Weiswampach	15:15–15:32	GS77	

[1] The images acquired at Bicherhaff were blurry due to high-velocity wind and hence were removed from the analysis.

Image preprocessing included orthomosaic generation, geometric correction, and co-registration across acquisition dates to enable pixel-level time-series analyses. Orthomosaics were generated using structure-from-motion photogrammetric processing workflows, including image alignment, construction of the dense point cloud and mesh, geometric optimization, and orthorectification. Since there was no ground control point across the study sites, the image-to-image registration tool was used in Quantum GIS (QGIS) software (version 3.8; Open Source Geospatial Foundation, Chicago, IL, USA) to allow for time-series analyses at the pixel-to-pixel level. Co-registration quality between acquisition dates was systematically verified to minimize spatial mismatch and ensure that spectral trajectories originated from comparable canopy areas across time.

As the methodology for disease severity estimation from UAV RGB imagery was detailed in [7], we briefly describe it here. A visual cryptography technique [33] was implemented to discriminate leaf areas diseased by WSR and WLR. Prior to analysis, a vegetation mask (Equation (1)) was applied to remove soil background effects, ensuring that spectral metrics were derived exclusively from canopy pixels. The equation for the vegetation mask was as follows:

$$\alpha = DN_{green} - DN_{blue} \text{ and } \beta = DN_{green} - DN_{red} \quad (1)$$

where DN_{green}, DN_{blue}, and DN_{red} are the digital numbers (DNs) of the green, blue, and red channels of the visible spectrum, respectively. Threshold values greater than 20 for both α and β allowed for a better characterization of canopy cover when visually comparing the preliminary estimates to corresponding RGB images [7,34]. A value of 20 was therefore kept for α and β.

To estimate UAV RGB imagery-derived WSR and WLR severities, we hypothesized that combinations of the primary RGB color channels can generate distinct spectral color codes under additive or subtractive color models. The theoretical basis of this color composite generation has been previously described by Hou [33]. In the additive color model, equal-intensity combinations of the red and green channels produce yellow tones. Thus, the WSR severity percentage was estimated by combining the red and green channels using the following equation [7]:

$$\text{WSRI} = [(\text{DN}_{\text{red}} + \text{DN}_{\text{green}})] > \Upsilon \quad (2)$$

where WSRI is the WSR index. A visual validation procedure was conducted by comparing the preliminary WSRI thresholding outputs with the corresponding RGB imagery. The threshold value of $\Upsilon = 400$ was selected since it minimized discrepancies in the delineation of WSR-affected regions between the WSRI-based thresholding results and the original RGB images.

WLR severity was quantified using the wheat leaf rust index (WLRI), computed as the ratio between dark brown and light brown color codes (Equation (3)). The dark brown color code was derived by subtracting the red channel from the green channel while applying double intensity weighting to the green component. For the light brown color code, the red and green channels were first combined additively with doubled intensity, after which the blue channel was subtracted from the resulting composite [7].

$$\text{WLRI} = [(2 \times \text{DN}_{\text{green}} - \text{DN}_{\text{red}})/(2 \times \text{DN}_{\text{red}} + 2 \times \text{DN}_{\text{green}} - \text{DN}_{\text{blue}})] < \delta \quad (3)$$

A visual validation procedure, analogous to that used for the WSRI, was performed to determine the optimal thresholding result for the WLRI. The threshold value of $\delta = 0.3$ was retained because it produced the smallest difference in the area of WLR-detected boundaries between the WLRI-based thresholding outputs and the original RGB images.

By reducing the effects of soil reflectance, non-vegetated surfaces, mixed pixels, and geometric displacement on temporal spectral trajectories, changes in the green–red spectral slope can be interpreted as a consistent within-season physiological signal rather than an artifact of acquisition geometry or variable illumination. Given that the primary objective of this study was to analyze relative temporal changes in canopy spectral dynamics, the methodological framework emphasized within-season temporal consistency. The green–red spectral slope was therefore interpreted as a relative indicator of canopy physiological dynamics rather than an atmospherically corrected reflectance metric.

3.3. Operationalization of the SEWS Framework

3.3.1. Definition of the Spectral State Variable

To operationalize the SEWS framework, the green–red spectral slope was defined as the primary spectral state variable describing canopy physiological stability. This metric captures relative changes in reflectance between the green and red channels, which are strongly influenced by chlorophyll absorption and photosynthetic functionality. For each acquisition date and experimental plot, the spectral slope was computed at canopy level as the normalized difference between the DNs of the green and red spectral channels, averaged across vegetation pixels. This time-dependent metric was treated as a continuous variable representing the functional integrity of the crop canopy.

For each plot and acquisition date, the green–red spectral slope (GRS) was calculated as:

$$\text{GRS}_t = \frac{G_t - R_t}{G_t + R_t} \quad (4)$$

where GRS_t is the green–red spectral slope at image acquisition date t; G_t and R_t are the mean DN of the green and red spectral channels at image acquisition date t. Positive GRS values indicate stronger green dominance and higher canopy physiological integrity, whereas progressive reductions in GRS reflect flattening of the green–red spectral gradient associated with physiological destabilization.

The spectral flattening is expected to occur when chlorophyll absorption in the red region weakens and canopy reflectance changes due to chlorosis, pigment degradation, altered photosynthetic activity, or pathogen-induced physiological stress. Although other RGB spectral contrasts, including blue–green and red–blue combinations, can be informative in this context, the green–red spectral slope was selected because WSR and WLR primarily alter canopy reflectance dynamics along the green–red region of the visible spectrum.

3.3.2. Temporal Analysis of Spectral Dynamics

Spectral slope time series were constructed for each of the 192 experimental plots monitored across the four successive UAV acquisition dates, generating a high-resolution spatiotemporal dataset of canopy physiological dynamics. Temporal analyses emphasized changes in the green–red spectral slope over time, rather than isolated spectral values, enabling the detection of progressive canopy destabilization associated with the early stages of epidemic development. To characterize temporal destabilization dynamics, first-order temporal variations in the spectral slope were computed between successive UAV acquisition dates. The first-order temporal difference was calculated as follows:

$$\Delta GRS_t = GRS_t - GRS_{t-1} \quad (5)$$

where ΔGRS_t represents the temporal variation in green–red spectral slope between two consecutive UAV acquisition dates. GRS_{t-1} denotes the corresponding value at the preceding UAV acquisition date.

Because UAV acquisitions were not equally spaced in time, temporal variations were further standardized by the number of days separating consecutive acquisitions. This standardization ensured comparability of spectral decline rates across unequal observation intervals and avoided overestimating destabilization during longer acquisition gaps. The standardized temporal rate of spectral change was calculated as follows:

$$Rate_t = \frac{GRS_t - GRS_{t-1}}{Date_t - Date_{t-1}} \quad (6)$$

where $Date_t - Date_{t-1}$ represents the number of days between two consecutive UAV acquisitions. Negative ΔGRS_t values indicate a progressive flattening of the green–red spectral slope and are interpreted as evidence of physiological destabilization associated with the emergence of SEWS.

A spectral destabilization point is defined as the first UAV acquisition date at which the decline in the green–red spectral slope exceeded the baseline variability observed in disease-free or low-disease reference plots. A spectral destabilization point was assigned when ΔGRS_t (Equation (5)) becomes negative and its absolute magnitude exceeded the site-specific baseline threshold.

Because wheat canopies naturally undergo maturation and senescence during late developmental stages, care was taken to distinguish pathogen-induced spectral destabilization from normal phenological ageing. Site-specific baseline thresholds were therefore derived from the temporal variability observed in healthy or minimally infected reference plots during the early epidemic stages, while analyses were restricted to periods preceding advanced canopy maturity to minimize confounding effects from natural senescence. Natural canopy maturation was expected to produce gradual, progressive, and seasonally

coherent declines in the green–red spectral slope across plots. In contrast, pathogen-induced destabilization was characterized by an earlier onset, a steeper decline, and a more abrupt flattening of the spectral trajectory relative to healthy reference canopies. Accordingly, the interpretation of SEWS relied not only on the magnitude of spectral decline, but also on its timing, acceleration, and deviation from expected physiological senescence patterns.

Since UAV acquisitions were performed at discrete dates in the fields, the spectral destabilization point should not be interpreted as an instantaneous biological threshold, but rather as the earliest temporally detectable indication of progressive canopy physiological instability. This destabilization point therefore marks the onset of the pre-symptomatic early-warning phase within the SEWS framework and represents the transition from physiologically stable canopy conditions toward latent epidemic reorganization preceding visible symptom acceleration.

3.3.3. Identification of the Pre-Symptomatic Window

The pre-symptomatic window (PSW) was quantified as the interval between the spectral destabilization point and the epidemic transition point. The spectral destabilization point corresponds to the first UAV acquisition date at which the green–red spectral slope showed a decline exceeding baseline variability. The epidemic transition point was defined as the first observation date at which visually assessed disease severity exhibited sustained acceleration relative to the preceding observation interval. In this study, the epidemic transition point corresponded to the first moving-window center at which the absolute rolling correlation reached or exceeded the threshold $|r| \geq 0.6$. To avoid ambiguity associated with isolated short-term fluctuations or transient severity increases, a transition point was assigned only when the increase in disease severity persisted during the subsequent observation interval or was followed by continued epidemic progression. This criterion aimed at improving the robustness and reproducibility of the detection of epidemic transition across sites, cultivars, and fungicide treatments.

The rapid increase in disease severity was identified based on changes in the slope of disease severity time series, corresponding to epidemic acceleration. The PSW, expressed in days, was computed for each plot, site, and disease (Equation (7)).

$$PSW = T_{transition} - T_{destabilization} \quad (7)$$

where PSW is the estimated pre-symptomatic window; $T_{destabilization}$ denotes the date of the first notable decline in the green–red spectral slope exceeding baseline variability; and $T_{transition}$ denotes the date corresponding to the onset of sustained epidemic acceleration based on visually assessed disease severity.

Because UAV acquisitions and visual disease assessments were available at discrete dates, the PSW was reported as an estimated range rather than as an exact continuous value. This temporal discretization reflects the operational nature of UAV field monitoring and avoids overinterpretation of the exact timing of physiological transitions between consecutive acquisition dates. The PSW provides a quantitative estimate of the early-warning capacity of RGB spectral dynamics relative to conventional symptom-based assessments. Within the SEWS framework, the PSW corresponds to a transitional physiological phase during which latent host–pathogen interactions progressively destabilize canopy functioning before visible symptoms dominate canopy reflectance.

3.3.4. Decoupling Between Spectral Dynamics and Disease Severity

To test whether SEWSs represent independent physiological signals rather than early symptom proxies, correlations between spectral slope values and disease severity were evaluated separately for the pre-symptomatic and epidemic expansion phases. Weak

or non-significant correlations during the pre-symptomatic phase, followed by strong correlations after epidemic onset, were interpreted as evidence of temporal decoupling between physiological destabilization and visible symptom expression.

3.4. Statistical Analysis

The relationships between spectral metrics and disease severity were assessed through correlation analyses. Rolling (moving-window) correlation coefficients were computed to capture the temporal dynamics of the association between spectral signals and disease severity [35]. Specifically, Pearson's correlation coefficients were calculated within a sliding time window of fixed length, progressively shifted along the time series, allowing the detection of transient phases of coupling and decoupling between variables. Rolling correlations were computed using a centered 5-day moving window. Because disease severity exhibited low temporal variance during the earliest epidemic stages, rolling correlation coefficients in the pre-symptomatic phase were interpreted primarily as indicators of phase-dependent coupling instability rather than as conventional measures of association between variables. This approach enables the identification of early destabilization signals that are not observable through static correlation analyses.

Temporal trends in spectral slopes and disease severity were further analyzed using regression techniques to identify transition points and rates of change. Temporal trajectory illustrations were used to characterize phase-dependent spectral dynamics and epidemic transitions across sites, diseases, and fungicide treatments. These illustrations were based on aggregated plot-level trends rather than individual replicate series. Variability among plots was incorporated into aggregated analyses and statistical inference; however, overlaying full confidence intervals or error bands across all sites, dates, diseases, and fungicide treatments would have substantially degraded figure readability and obscured the phase-transition structure central to the SEWS framework. Plot-level variability was therefore not systematically displayed in the multi-panel figures to maintain visual clarity and facilitate comparison of transition dynamics. All analyses were conducted using R (version 4.4.1) [36] within the RStudio development environment (version 2026.1.2.418) [37].

4. Results

4.1. Temporal Dynamics of RGB Spectral Slopes and Disease Severity

Time-series analysis revealed distinct temporal trajectories between RGB-derived spectral dynamics and visually assessed disease severity across sites, cultivars, and treatments. While disease severity remained low and relatively stable during early phenological stages, the green–red spectral slope exhibited a consistent and progressive decline (Figure 3). The progressive flattening of the spectral slope was consistently observed across all experimental sites prior to the rapid increase in disease severity, although with site-specific temporal dynamics. At each site, this spectral attenuation preceded the onset of epidemic acceleration, with variations in the timing and magnitude of the signal reflecting local environmental conditions, canopy structure, and disease pressure. Specifically, the decline in the green–red spectral slope occurred before any notable increase in visually assessed disease severity (Figure 3), thereby indicating an early loss of canopy physiological stability.

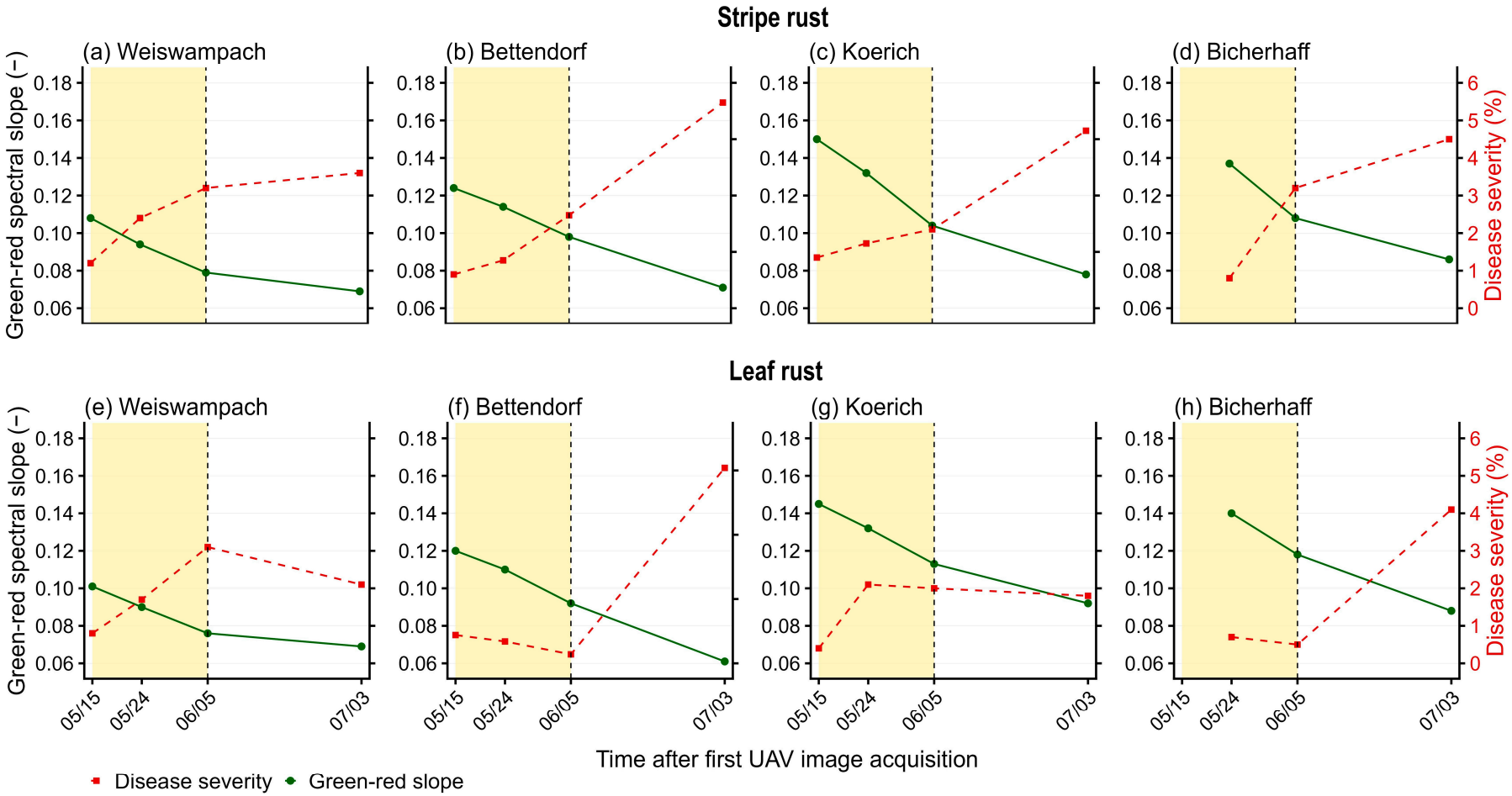


Figure 3. Site-specific temporal dynamics of green–red spectral slope and disease severity in wheat stripe rust (**a**–**d**) and leaf rust (**e**–**h**) epidemics. Solid green lines show the green–red spectral slope; red dashed lines show visually assessed disease severity. The yellow shaded area indicates the pre-symptomatic window, and the dashed vertical line marks the estimated transition point.

While the duration of this pre-symptomatic phase for each disease varied across sites, the underlying pattern remained robust, supporting the hypothesis that spectral dynamics capture early physiological destabilization processes that are not yet detectable through conventional visual assessments (Table 2). Importantly, spectral changes occurred while visually assessed disease severity remained below commonly used decision thresholds (≤5–10%).

Table 2. Site-specific estimates of the pre-symptomatic destabilization phase for wheat stripe rust and wheat leaf rust derived from UAV RGB time series.

Disease	Site	Spectral Destabilization Detected Between UAV Dates	Visible Severity Acceleration Detected by Field Observations	Estimated Duration of Pre-symptomatic Phase (Days) *
Wheat stripe rust	Bettendorf	Between 24 May and 5 June	Before 3 July	7–14
	Bicherhaff	Between 24 May and 5 June	Before 3 July	7–14
	Koerich	Between 24 May and 5 June	Before 3 July	7–14
	Weiswampach	Between 5 June and 3 July	By 3 July	7–14
Wheat leaf rust	Bettendorf	Between 5 June and 3 July	By 3 July **	5–10
	Bicherhaff	Between 5 June and 3 July	By 3 July	5–10
	Koerich	Between 5 June and 3 July	By 3 July	5–10
	Weiswampach	Between 5 June and 3 July	By 3 July	5–10

* Durations are reported as estimated ranges because UAV observations were acquired at discrete dates rather than continuously. ** July 3 was selected because it was the final UAV acquisition date available for paired UAV–field analysis. Although disease monitoring can continue beyond this date in operational surveillance, the present SEWS analysis was restricted to synchronized UAV and visual assessment dates. Consequently, July 3 should be interpreted as the last remotely sensed observation point rather than the biological endpoint of the epidemic.

In some site-specific leaf rust trajectories, particularly in panels where disease severity decreased or fluctuated after the estimated transition point, disease severity did not increase monotonically. This pattern likely reflects a combination of fungicide effects, canopy senescence, changing visibility of infected leaves within the canopy, observer-related variability, and spatial heterogeneity in symptom expression. Therefore, the epidemic transition point should be interpreted as the onset of spectral–epidemiological reorganization and sustained epidemic acceleration at the site or trajectory level, rather than as a guarantee of monotonic severity increase in every individual curve. Note that across all sites, disease-free or minimally infected reference plots did not exhibit comparable early inflection points or abrupt declines in the green–red spectral slope during the same observation periods. This contrast further supports the interpretation that the detected spectral destabilization was primarily associated with pathogen-induced physiological perturbation rather than normal canopy development or natural late-season senescence alone.

Table 2 provides site-specific estimates of the pre-symptomatic destabilization phase for WSR and WLR. Across all sites, the decline in the green–red spectral slope preceded the subsequent increase in visible disease severity. However, the duration of this phase was not identical across diseases or sites. The PSW was relatively longer for WSR (7–14 days) than for WLR (5–10 days), highlighting disease-specific differences in the temporal expression of canopy physiological destabilization.

Figure 4 illustrates the temporal dynamics of the green–red spectral slope and visually assessed disease severity for WSR and WLR. Across sites, spectral destabilization consistently preceded epidemic acceleration. In contrast, disease-free control plots showed no comparable monotonic decline or early inflection in the green–red spectral slope, suggesting that the observed temporal patterns were not attributable to normal canopy development or late-season senescence alone. These temporal dynamics support the hypothesis that RGB-derived spectral trajectories capture anticipatory physiological responses before substantial symptom accumulation. Rather than serving solely as static proxies for visible

disease severity, green–red spectral slopes may reflect early dynamic changes in canopy condition that precede disease intensification.

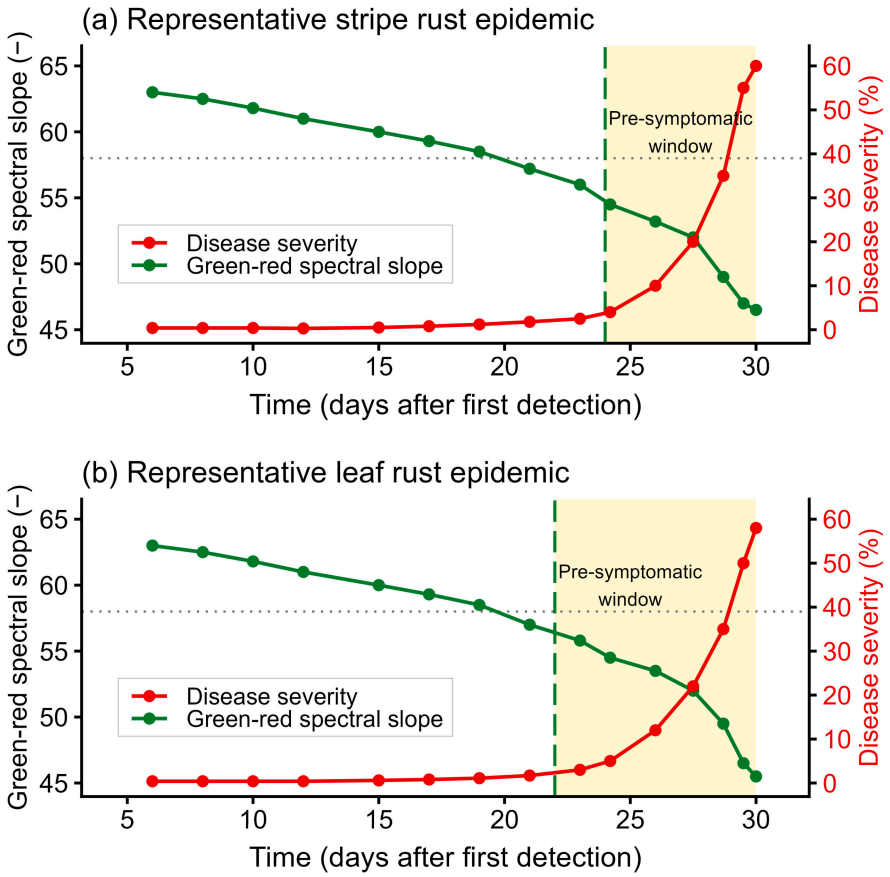


Figure 4. Temporal dynamics of the green–red spectral slope derived from UAV-based RGB imagery and visually assessed disease severity for representative wheat stripe rust (**a**) and wheat leaf rust (**b**) epidemics. The dashed vertical line indicates the spectral destabilization point, marking the onset of spectral early-warning signals (SEWS). The yellow shaded area indicates the pre-symptomatic window, during which pronounced spectral destabilization occurs before rapid visible disease increases. Dashed horizontal lines represent the baseline spectral slope threshold (≈57), calculated as the mean green–red spectral slope across the first UAV imagery acquisition dates at the study sites.

4.2. Identification of the Spectral Destabilization Point

A phase-space representation of the relationship between the green–red spectral slope and disease severity is presented in Figure 5. The trajectory can be interpreted as a chronological pathway from early-season physiologically stable canopy conditions (high spectral slope) to late-stage destabilized states (low spectral slope). These dynamics highlight an initial phase characterized by a marked decline in spectral slope occurring under very low disease severity (<5%). This PSW was followed by a rapid increase in disease severity once a critical spectral threshold was approached, reflecting a transition toward epidemic amplification. This phase-space representation simplified the interpretation of epidemic progression by distinguishing an early physiological destabilization regime from the subsequent symptom-dominated epidemic phase. Rather than increasing simultaneously with disease severity, spectral changes preceded epidemic amplification and followed a temporally ordered destabilization trajectory. The resulting trajectory had a nonlinear structure, with a clear temporal decoupling between spectral dynamics and disease severity during the early stages, followed by a progressive re-coupling as the epidemic intensified. The monotonic progression observed along the trajectory supports the interpretation of spectral

slope decline as a leading indicator of canopy destabilization. These empirical dynamics are consistent with the theoretical expectations of SEWS, reinforcing their capacity to capture pre-critical transitions and to provide actionable early-warning information prior to visible symptom escalation.

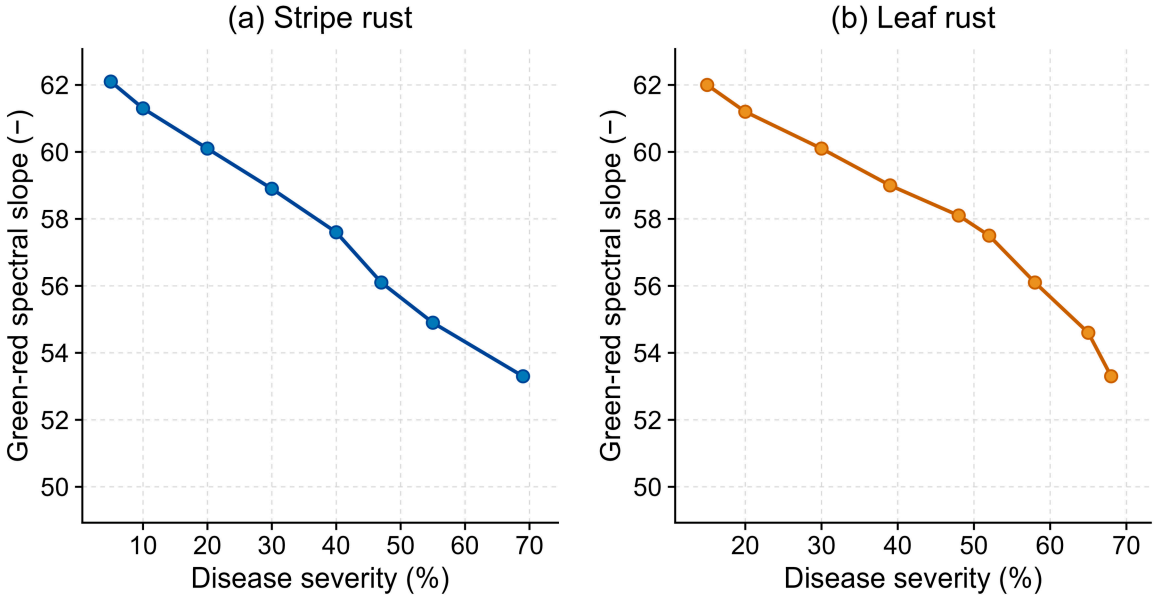


Figure 5. Phase-space relationship between green–red spectral slope and disease severity during (**a**) stripe rust and (**b**) leaf rust epidemics.

4.3. Emergence of SEWS Prior to Epidemic Acceleration

4.3.1. SEWS Emerge Before Visible Disease Escalation

The observed spectral dynamics satisfy the operational criteria of SEWS, as they emerged before visible epidemic amplification and while visually assessed disease severity remained below conventional intervention thresholds (5–10%). At this stage, the green–red spectral slope had already declined by approximately 60–80% relative to baseline values, indicating substantial canopy physiological destabilization despite limited symptom expression (Figure 6). This pre-symptomatic phase therefore reflects a state in which RGB-derived spectral dynamics captured latent host–pathogen interactions before overt symptom dominance. As the epidemic progressed, disease severity increased rapidly and spectral–severity coupling strengthened, marking the transition from an anticipatory spectral signal to a symptom-associated response.

Quantitative and statistical characterizations of SEWS across the pre-symptomatic and epidemic phases are presented in Table 3. Overall, the pre-symptomatic phase was distinguished by low visually assessed disease severity (3–8%), a marked reduction in green–red spectral slope relative to baseline conditions (−60 to −80%), and weak or unstable coupling between spectral dynamics and disease severity (r ranging from −0.10 to 0.25) (Table 3). In contrast, the epidemic phase was associated with substantially higher disease severity (25–45%), a stronger reduction in spectral slope (−80 to −90%), and markedly stronger spectral–severity coupling (r = 0.70–0.90) (Table 3). The estimated early-warning lead time ranged from 5 to 14 days, confirming that SEWS emerged significantly before epidemic amplification. Taken together, these results indicate that the pre-symptomatic phase corresponds to a distinct dynamical regime characterized by physiological destabilization prior to strong symptom expression, whereas the epidemic phase reflects the progressive re-coupling of spectral and pathological signals.

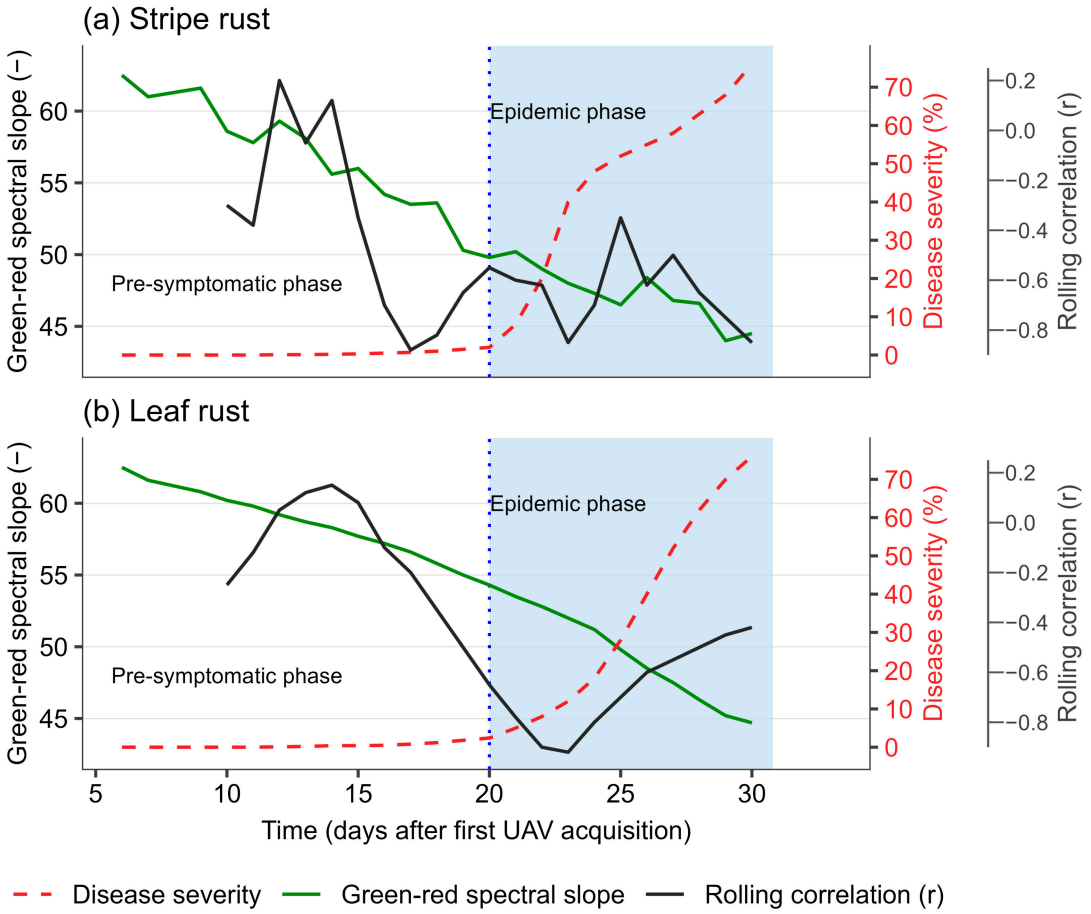


Figure 6. Phase-dependent emergence of SEWS preceding wheat stripe rust (**a**) and wheat leaf rust (**b**) epidemics. The vertical blue dotted line marks the epidemic transition point. The period preceding the transition point is the pre-symptomatic phase, during which spectral destabilization is already detectable while disease severity remains low. The blue shaded area corresponds to the epidemic phase, characterized by a rapid increase in disease severity and stronger spectral–severity coupling. The trajectories were derived from the pooled data.

Table 3. Quantitative and statistical characterization of SEWS during pre-symptomatic and epidemic phases. Pooled observations from the four study sites were used.

Variable Tested	Pre-Symptomatic Phase	Epidemic Phase	Statistical Test	Test Result
Disease severity (%) at SEWS activation	3–8	25–45	Mann–Whitney U	$p < 0.001$
Green–red spectral slope (relative change, %)	−60 to −80	−80 to −90	Wilcoxon signed-rank	$p < 0.001$
Correlation (spectral slope vs. severity, r)	−0.10 to 0.25	0.70 to 0.90	Fisher's z-test	$z > 3.5$; $p < 0.001$
Temporal lead time (days)	5–14	—	One-sample *t*-test vs. 0	$p < 0.001$
Phase-dependent coupling strength	Weak/unstable	Strong/stable	Permutation test	$p < 0.01$

4.3.2. Temporal Decoupling Between Spectral Dynamics and Disease Severity

During the SEWS phase, rolling correlation analysis revealed a marked and temporally structured decoupling between spectral dynamics and disease severity (Figure 6). Correlation values remained weak and unstable during the early phase, indicating that spectral alterations captured physiological destabilization before substantial visible symptom expression. As the epidemic progressed, correlation values became stronger in magnitude, reflecting a progressive re-coupling between canopy spectral degradation and disease severity once visible symptoms increasingly dominated canopy reflectance. Correlation coefficients were initially slightly positive, then declined sharply to strongly negative values during the pre-symptomatic window, before gradually increasing toward weaker negative values as disease severity accelerated. This trajectory reflects a transient regime in which physiological canopy responses preceded visible symptom expression, producing an apparent inversion of the spectral–severity relationship. Such dynamics support the interpretation of SEWS as indicators of incipient epidemic destabilization rather than symptom-driven reflectance responses.

Rolling correlations during the pre-symptomatic phase should be interpreted cautiously because visually assessed disease severity showed limited temporal variance while the green–red spectral slope was already changing. Under such conditions, correlation coefficients may fluctuate and appear unstable, even when biologically meaningful spectral destabilization is occurring. Therefore, the key diagnostic feature was not the absolute sign or short-term increase in the early rolling correlation, but the phase-dependent transition from weak or unstable coupling before symptom development to stronger and more persistent coupling after epidemic acceleration.

4.3.3. Quantification of SEWS Lead Time

Table 4 provides an overview of the range of estimated lead times as well as the corresponding changes in spectral slope for WSR and WLR. Stripe rust epidemics generally exhibited longer lead times than leaf rust: 7 to 14 days versus 5 to 10 days (Table 4), which can be explained by differences in host–pathogen interaction dynamics. The consistent range found at all four study sites indicates that the aggregated signal was robust to differences in cultivar susceptibility, site conditions, and fungicide regimes. While these sources of heterogeneity influenced the duration and magnitude of the early-warning signal, they did not modify the overall temporal pattern whereby spectral destabilization preceded visible disease escalation. This lead time represents a critical operational advantage by enabling disease monitoring systems to shift from reactive detection toward anticipatory surveillance. Detecting subtle physiological changes while visible symptom expression remains limited and below conventional intervention thresholds provides a strategic window for earlier intervention, optimized treatment timing, and improved risk management under field conditions.

Table 4. Quantification of the pre-symptomatic destabilization phase derived from UAV-based RGB imagery.

Disease	Lead Time (Days)	Reduction in Spectral Slope Magnitude (%)	Disease Severity at Destabilization (%)
Wheat stripe rust	7–14	65–80	<5
Wheat leaf rust	5–10	60–75	<10

4.4. Decoupling Between Spectral Dynamics and Visible Disease Severity

For both diseases, rolling-correlation analyses based on the pooled observations from the four study sites revealed a clear phase-dependent decoupling between spectral dynamics and disease severity during the pre-symptomatic stage (Figure 7a,b). In this early phase, the rolling correlation between the green–red spectral slope and visually assessed disease severity remained weak or unstable in magnitude, generally below the absolute threshold defining epidemic transition ($|r| < 0.6$). This indicates that spectral variations primarily captured early canopy physiological destabilization rather than the progression of visible symptoms. Although the exact temporal trajectories differed among sites, the overall analysis revealed a consistent pattern for both diseases. After the epidemic transition point, correlations became persistently negative and stronger in magnitude (Figure 7). This shift reflects a progressive strengthening of the inverse coupling between canopy spectral degradation and disease severity, indicating that spectral metrics evolved from leading early-warning indicators during the pre-symptomatic phase to more reliable proxies of disease severity once visible symptoms increasingly dominated canopy reflectance.

4.5. Consistency Across Sites, Cultivars, and Treatments

The pre-symptomatic phase was consistently detected across all experimental sites and different fungicide regimes (Figure 8). The pre-symptomatic phase occurred before the epidemic transition point across sites, diseases, and fungicide treatments. At each site, the onset of spectral destabilization preceded the rapid increase in disease severity. Under both fungicide-treated and untreated conditions, a progressive decline in the green–red spectral slope was observed during early epidemic stages, while disease severity remained low (Figure 8). This pattern was associated with weak or unstable spectral–severity correlations, indicating a decoupling between physiological disruption and visible symptom expression. Following the epidemic transition, a rapid increase in disease severity was observed, accompanied by a strengthening of spectral–severity coupling.

While fungicide treatments delayed the timing of epidemic acceleration and reduced overall disease severity, they did not suppress the emergence of the pre-symptomatic phase. Instead, this phase remained detectable across management regimes, though its duration and intensity varied. Although fungicide treatments reduced final disease severity, they did not suppress the early spectral destabilization signal, suggesting that SEWS captured early physiological responses preceding effective disease control. This consistency supports the robustness of the SEWS framework and its applicability under a broad range of field conditions.

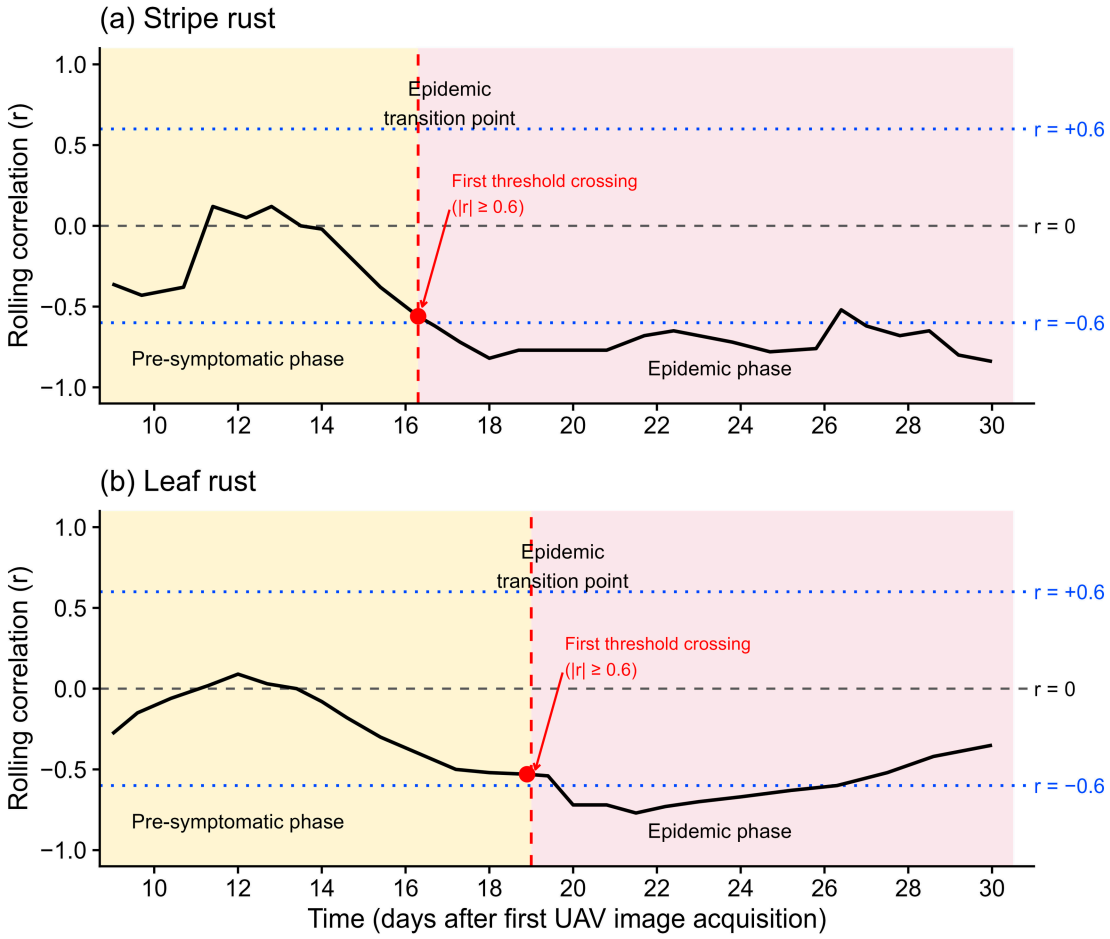


Figure 7. Phase-dependent evolution of rolling correlations between green–red spectral slope and visually assessed disease severity for wheat stripe rust (**a**) and leaf rust (**b**). The black line represents the rolling correlation coefficient (r) calculated over successive moving windows along the aggregated temporal series pooled from the four study sites. The red dashed vertical line marks the epidemic transition point, defined here as the first time at which the absolute correlation magnitude reached the threshold $|r| \geq 0.6$. Blue dotted horizontal lines indicate the positive and negative correlation thresholds ($r = +0.6$ and $r = -0.6$). The yellow shaded area corresponds to the pre-symptomatic phase, during which rolling correlations remained weak or unstable in magnitude. The pink shaded area corresponds to the epidemic phase, characterized by stronger and more persistent coupling between spectral dynamics and disease severity.

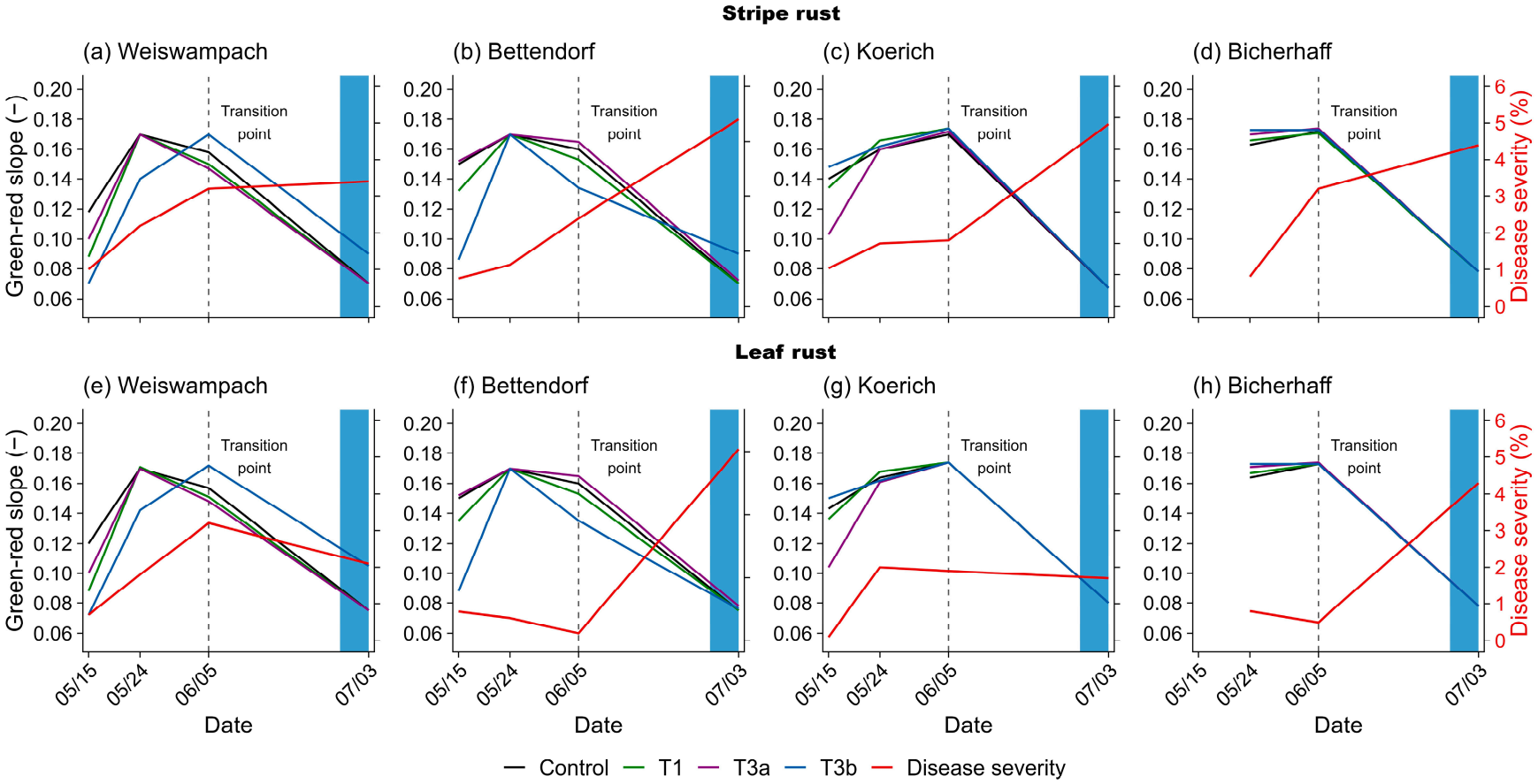


Figure 8. Site-specific temporal dynamics of green–red spectral slope and disease severity in stripe rust (**a**–**d**) and leaf rust (**e**–**h**) for different fungicide treatments. The fungicide treatments comprised a control (untreated plots), T1 (a single fungicide application), T3a (three fungicide applications, with the final spray applied at GS59), and T3b (three fungicide applications, with the final spray applied at GS69). The dashed vertical line marks the epidemic transition point. The dark-blue shaded area indicates the epidemic phase after visible disease acceleration. Temporal trajectories represent aggregated plot-level responses across replicated experimental plots within each fungicide treatment. Error bars were omitted to preserve the readability of treatment-dependent temporal dynamics across sites.

5. Discussion

5.1. From Symptom Detection to Physiological Destabilization: A Paradigm Shift

The study demonstrated that UAV-based RGB imagery can detect a pre-symptomatic phase of rust disease epidemics in winter wheat, characterized by progressive destabilization of canopy spectral dynamics well before the onset of visible symptoms. This finding challenges the prevailing symptom-oriented paradigm in plant disease remote sensing, in which spectral signals are typically interpreted primarily as proxies for lesion development or chlorosis [5,9]. Although RGB and multispectral imagery have proven effective in assessing disease severity after symptom manifestation [6,8,10], the temporal aspects of spectral changes preceding the onset of epidemic expansion have received limited attention. By interpreting the green–red spectral slope as a state variable of canopy physiological integrity, our results reveal that wheat rust epidemics follow a two-stage spectral trajectory: an early physiological destabilization phase followed by a symptom-dominated epidemic phase.

5.2. SEWS and Critical Transitions in Crop Pathosystems

The SEWS proposed in this study aligns closely with theoretical expectations from critical transition and resilience theory. In complex ecological and climatic systems, early-warning signals commonly manifest as changes in slopes, variance, or correlation structure prior to regime shifts [19–21]. Our results provide empirical evidence that WSR and WLR epidemics exhibited similar dynamics. The marked flattening of the green–red spectral slope observed 5 to 14 days before epidemic acceleration reflects a loss of physiological resilience at the canopy level. During this pre-symptomatic window, rolling correlations between spectral dynamics and disease severity remain weak or unstable, indicating that the spectral signal is not yet driven by visible damage. Only after the epidemic transition does the spectral signal become strongly coupled to disease severity, confirming that RGB-based metrics transition from early-warning indicators to conventional symptom proxies. This phase-dependent behavior is consistent with nonlinear epidemic models that predict threshold-driven dynamics in plant disease systems [18,38–41].

5.3. Linking Spectral Destabilization to Host–Pathogen Interactions

From a physiological perspective, the early destabilization of the green–red spectral slope is consistent with well-documented responses of wheat to biotrophic rust infection. Early infection stages are known to disrupt chlorophyll efficiency, photosynthetic capacity, and carbon allocation before extensive chlorosis becomes visible [22]. Experimental and modeling studies have shown that rust pathogens impose a significant metabolic burden on host tissues during latent infection phases, reducing photosynthetic performance and accelerating physiological exhaustion prior to visible symptom expression [42]. Because reflectance in the red and green bands is strongly governed by chlorophyll absorption, the green–red spectral slope appears particularly sensitive to early physiological perturbations affecting canopy functioning. However, it cannot be entirely excluded that part of the observed spectral changes may also be influenced by fungal biomass development within leaf tissues, particularly during the early stages of infection when visual symptoms remain limited.

Fungal colonization can alter internal leaf structure and optical properties, potentially contributing to modifications in reflectance independently of, or in conjunction with, host physiological responses. Nevertheless, the temporal dynamics observed in this study, characterized by a progressive spectral decline occurring prior to any substantial increase in visible disease severity, suggest that the dominant signal captured by the green–red spectral slope reflects early host physiological destabilization rather than solely fungal biomass accumulation.

While fungal biomass may contribute to the observed spectral variability, the consistent temporal decoupling between spectral dynamics and visible symptoms supports the interpretation of the green–red spectral slope as an integrative indicator of pre-symptomatic canopy destabilization. Our results therefore support a mechanistic interpretation in which SEWS reflect host physiological destabilization rather than pathogen biomass or lesion density, a distinction that is critical for the correct interpretation of remote sensing signals in disease monitoring.

5.4. Robustness of SEWS Across Sites, Cultivars, and Management Regimes

A key strength of the SEWS framework lies in its robustness across heterogeneous conditions, as demonstrated by the consistency of spectral destabilization patterns observed across experimental sites and management regimes. The pre-symptomatic phase was systematically detected at each site, with a comparable temporal structure characterized by an early decline in the green–red spectral slope preceding the rapid increase in disease severity. This pattern was observed across varying fungicide treatments and different cultivars, though the timing and magnitude of the spectral signal varied depending on local environmental conditions and canopy protection levels. Moreover, the onset of spectral destabilization occurred prior to epidemic acceleration, indicating that SEWSs capture a generalizable physiological response rather than a site- or treatment-specific artifact.

Fungicide applications reduced disease severity but did not suppress the early spectral destabilization phase. This conclusion is based on comparisons between untreated control plots and fungicide-treated plots, including both preventive and curative application regimes implemented within the experimental design. While curative treatments were applied after the onset of visible symptoms, in accordance with integrated pest management principles, preventive applications were also included to explore a wider range of canopy protection scenarios. Across these treatment modalities, a consistent decline in the green–red spectral slope was observed prior to the increase in visually assessed disease severity, indicating that early spectral destabilization occurred irrespective of fungicide timing.

The physiological changes associated with early disease infection occur before visible symptoms appear and before fungicide treatments are applied. This highlights the value of SEWS as early warning signals in disease management strategies and its relevance for anticipatory monitoring rather than post hoc assessment. Similar decoupling between early physiological stress and visible symptom expression has been reported in controlled pathosystem experiments [43]. Such robustness is essential for operational deployment and distinguishes SEWS from many disease indices whose performance deteriorates under varying agronomic conditions [5,7].

5.5. Implications for Precision Agriculture and Early Disease Management

The identification of a quantifiable early-warning lead time of 5–14 days has major implications for precision agriculture. This temporal window offers a concrete opportunity to shift disease management from reactive intervention to anticipatory decision-making, potentially improving fungicide timing, reducing unnecessary applications, and limiting yield losses. Since the SEWS framework relies solely on UAV-based RGB imagery, it can be deployed using widely available platforms without requiring hyperspectral sensors. This makes it especially useful for disease monitoring operations and in areas where advanced sensors are not accessible [6,28,29].

5.6. Limitations of the Study

While the present findings establish a robust empirical basis for RGB-derived spectral early warning signals (SEWS) in wheat rust epidemics, several limitations warrant consideration. The SEWS were validated specifically for WSR and WLR. Its applicability to other

crop–pathogen systems may require further testing. Indeed, necrotrophic pathogens or diseases that cause rapid tissue collapse may display spectral–physiological relationships that differ from those observed in this study.

This framework relied exclusively on UAV-based RGB imagery and relative temporal spectral dynamics, without the integration of complementary physiological sensing approaches. The spectral response could still have been affected by variation in illumination, seasonal climatic conditions, and cultivar susceptibility. The incorporation of calibrated reflectance panels, radiometric normalization procedures, hyperspectral sensing, thermal imagery, chlorophyll fluorescence, or radar observations may help to refine the mechanistic interpretation of SEWS and could improve the reproducibility of the framework.

UAV acquisitions were conducted at discrete observation intervals rather than through continuous monitoring, which constrained the temporal precision of estimated lead times and transition points. The pre-symptomatic detection window should accordingly be interpreted as an operational estimate of early-warning capacity rather than an exact physiological transition duration. Increasing acquisition frequency—and, where feasible, integrating near-continuous proximal or satellite sensing—would substantially improve temporal resolution and sharpen detection of the nonlinear dynamics that preceded epidemic amplification. These methodological advances would position the SEWS framework for deployment as a scalable, mechanistically grounded tool for precision disease management in cereal crops.

Disease severity was assessed through standardized visual scoring, which, despite remaining the operational reference in large-scale epidemiological field studies, carries inherent uncertainties arising from observer subjectivity, heterogeneous lesion distribution, canopy occlusion, and reduced symptom visibility during early epidemic stages [44,45]. Critically, visual assessment was not complemented by direct biochemical or molecular measurements (e.g., chlorophyll fluorescence, pigment composition, and pathogen biomass quantification). The physiological interpretation of SEWS should therefore be understood as inference grounded in established wheat rust–host interaction theory and known RGB spectral behavior, rather than as direct biochemical validation of canopy physiological collapse. This distinction does not diminish the operational utility of the framework, but it underscores the need for mechanistic validation in future work.

The temporal decoupling observed between spectral destabilization and visible symptom expression strongly implicates latent physiological perturbation—occurring prior to major lesion accumulation—as the primary driver of the detected RGB dynamics. Nevertheless, without independent physiological validation, a partial contribution from early fungal biomass development or subtle infection-induced structural modifications within leaf tissues cannot be formally excluded. Resolving this ambiguity represents a priority for subsequent investigations. We advocate for integrated multi-sensor campaigns combining UAV RGB monitoring with chlorophyll fluorescence imaging, hyperspectral and thermal sensing, gas-exchange analyses, pigment quantification, and laboratory-based pathogen biomass assays. Such a framework would provide the mechanistic resolution necessary to attribute pre-symptomatic spectral signals to specific physiological processes and to generalize the SEWS concept across pathosystems and environments.

6. Conclusions

By introducing and validating the concept of spectral early-warning signals (SEWS), this study shows that a progressive flattening of the green–red spectral slope consistently preceded epidemic acceleration by 5 to 14 days, while disease severity remained below conventional intervention thresholds. During the pre-symptomatic window, spectral dynamics were decoupled from the expression of visible symptoms. This indicates that SEWS

captured the collapse of host physiology, rather than merely tracking lesion accumulation. As the disease progresses, spectral signals re-couple with disease severity, marking the transition to the phase of symptom-dominated epidemic expansion. The phase-dependent behavior observed in RGB spectral dynamics established these measurements as process-informed early-warning indicators, rather than as static proxies of disease severity. This distinction enhances the value of low-cost RGB remote sensing, transforming its role from a diagnostic tool to a predictive, process-informed sensor for monitoring crop disease dynamics. The SEWS framework relies exclusively on widely accessible RGB imagery, offering a scalable and operationally realistic pathway for anticipatory disease surveillance and improved precision agriculture strategies. While this study focuses on wheat rust epidemics, the underlying methodological framework is transferable to other crop–pathogen systems where physiological stress occurs prior to the appearance of visible damage.

Supplementary Materials: The following supporting information can be downloaded at: https://www.mdpi.com/article/10.3390/rs18111769/s1, Table S1: Agronomic details for winter wheat plots used at the experimental sites in the Grand Duchy of Luxembourg for the cropping season 2018–2019.

Author Contributions: Conceptualization, M.E.J. and L.K.; methodology, M.E.J.; software, M.E.J.; validation, M.E.J., L.K. and M.B.; formal analysis, M.E.J.; investigation, M.E.J. and L.K.; resources, M.E.J.; data curation, M.E.J.; writing—original draft preparation, M.E.J.; writing—review and editing, L.K., J.P. and M.B.; visualization, M.E.J. and J.P.; supervision, L.K.; project administration, M.B.; funding acquisition, M.B. All authors have read and agreed to the published version of the manuscript.

Funding: The present research was funded by the Ministry of Agriculture, Food and Viticulture of the Grand Duchy of Luxembourg through the project Sentinelle.

Data Availability Statement: The data presented in this study are available on reasonable request from Dr Moussa El Jarroudi (Email: meljarroudi@uliege.be).

Acknowledgments: We acknowledge the financial support of the Ministry of Agriculture, Food and Viticulture of the Grand Duchy of Luxembourg. We thank Ramin Heidarian Dehkordi, Doriane Dam, Marine Pallez-Barthel, Mohammed Sallah Abdoulhamid, Malika Yazza, Fouad Zouhir, Marie Dufrasne, Mathieu Almeida, Chloé Dupuis, and Martin Vanrykel for their technical assistance. We thank Guy Reiland and Serge Heuschling for organizational support. During the preparation of this manuscript/study, the authors used ChatGPT based on the GPT-5.3 model to generate Figure 1. The authors have reviewed and edited the output and take full responsibility for the content of this publication.

Conflicts of Interest: The authors declare no conflicts of interest.

Abbreviations

The following abbreviations are used in this manuscript:

CIVE	Color Index of Vegetation Extraction
ExG	Excess Green index
PSW	Pre-symptomatic window
RGB	Red–Green–Blue
UAV	Unmanned aerial vehicle
SEWS	Spectral Early-Warning Signals
WLR	Wheat leaf rust
WLRI	WLR index
WSR	Wheat stripe rust
WSRI	WSR index

References

1. Oerke, E.C. Crop losses to pests. *J. Agric. Sci.* **2006**, *144*, 31–43. [CrossRef]
2. Savary, S.; Willocquet, L.; Pethybridge, S.J.; Esker, P.; McRoberts, N.; Nelson, A. The global burden of pathogens and pests on major food crops. *Nat. Ecol. Evol.* **2019**, *3*, 430–439. [CrossRef]
3. Hovmøller, M.S.; Walter, S.; Justesen, A.F. Escalating threat of wheat rusts. *Science* **2010**, *329*, 369. [CrossRef]
4. Beddow, J.M.; Pardey, P.G.; Chai, Y.; Hurley, T.M.; Kriticos, D.J.; Braun, H.-J.; Park, R.F.; Cuddy, W.S.; Yonow, T. Research investment implications of shifts in the global geography of wheat stripe rust. *Nat. Plants* **2015**, *1*, 15132. [CrossRef] [PubMed]
5. Mahlein, A.-K. Plant disease detection by imaging sensors—Parallels and specific demands for precision agriculture and plant phenotyping. *Plant Dis.* **2016**, *100*, 241–251. [CrossRef]
6. Zhang, N.; Yang, G.; Pan, Y.; Yang, X.; Chen, L.; Zhao, C. A review of advanced technologies and development for hyperspectral-based plant disease detection in the past three decades. *Remote Sens.* **2020**, *12*, 3188. [CrossRef]
7. Heidarian Dehkordi, R.; El Jarroudi, M.; Kouadio, L.; Meersmans, J.; Beyer, M. Monitoring wheat leaf rust and stripe rust in winter wheat using high-resolution UAV-based red-green-blue imagery. *Remote Sens.* **2020**, *12*, 3696. [CrossRef]
8. Kouadio, L.; El Jarroudi, M.; Belabess, Z.; Laasli, S.-E.; Roni, M.Z.K.; Amine, I.D.I.; Mokhtari, N.; Mokrini, F.; Junk, J.; Lahlali, R. A review on UAV-based applications for plant disease detection and monitoring. *Remote Sens.* **2023**, *15*, 4273. [CrossRef]
9. Bock, C.H.; Poole, G.H.; Parker, P.E.; Gottwald, T.R. Plant disease severity estimated visually, by digital photography and image analysis, and by hyperspectral imaging. *Crit. Rev. Plant Sci.* **2010**, *29*, 59–107. [CrossRef]
10. Mahlein, A.-K.; Oerke, E.-C.; Steiner, U.; Dehne, H.-W. Recent advances in sensing plant diseases for precision crop protection. *Eur. J. Plant Pathol.* **2012**, *133*, 197–209. [CrossRef]
11. Lelong, C.C.D.; Burger, P.; Jubelin, G.; Roux, B.; Labbé, S.; Baret, F. Assessment of unmanned aerial vehicles imagery for quantitative monitoring of wheat crop in small plots. *Sensors* **2008**, *8*, 3557–3585. [CrossRef]
12. Woebbecke, D.M.; Meyer, G.E.; Von Bargen, K.; Mortensen, D.A. Color indices for weed identification under various soil, residue, and lighting conditions. *ASAE Trans.* **1995**, *38*, 259–269. [CrossRef]
13. Kataoka, T.; Kaneko, T.; Okamoto, H.; Hata, S. Crop growth estimation system using machine vision. In Proceedings of the 2003 IEEE/ASME International Conference on Advanced Intelligent Mechatronics (AIM 2003), Kobe, Japan, 20–24 July 2003; Volume 1072, pp. b1079–b1083.
14. Wang, Y.; Yang, Z.; Kootstra, G.; Khan, H.A. The impact of variable illumination on vegetation indices and evaluation of illumination correction methods on chlorophyll content estimation using UAV imagery. *Plant Methods* **2023**, *19*, 51. [CrossRef]
15. Barbedo, J.G.A. A review on the use of unmanned aerial vehicles and imaging sensors for monitoring and assessing plant stresses. *Drones* **2019**, *3*, 40. [CrossRef]
16. Zarco-Tejada, P.J.; Camino, C.; Beck, P.S.A.; Calderon, R.; Hornero, A.; Hernández-Clemente, R.; Kattenborn, T.; Montes-Borrego, M.; Susca, L.; Morelli, M.; et al. Previsual symptoms of *Xylella fastidiosa* infection revealed in spectral plant-trait alterations. *Nat. Plants* **2018**, *4*, 432–439. [CrossRef]
17. Jeger, M.J.; Pautasso, M.; Holdenrieder, O.; Shaw, M.W. Modelling disease spread and control in networks: Implications for plant sciences. *New Phytol.* **2007**, *174*, 279–297. [CrossRef] [PubMed]
18. Cunniffe, N.J.; Koskella, B.; Metcalf, C.J.E.; Parnell, S.; Gottwald, T.R.; Gilligan, C.A. Thirteen challenges in modelling plant diseases. *Epidemics* **2015**, *10*, 6–10. [CrossRef] [PubMed]
19. Scheffer, M.; Bascompte, J.; Brock, W.A.; Brovkin, V.; Carpenter, S.R.; Dakos, V.; Held, H.; van Nes, E.H.; Rietkerk, M.; Sugihara, G. Early-warning signals for critical transitions. *Nature* **2009**, *461*, 53–59. [CrossRef]
20. Lenton, T.M. Early warning of climate tipping points. *Nat. Clim. Change* **2011**, *1*, 201–209. [CrossRef]
21. Dakos, V.; Carpenter, S.R.; van Nes, E.H.; Scheffer, M. Resilience indicators: Prospects and limitations for early warnings of regime shifts. *Philos. Trans. R. Soc. Lond. Ser. B* **2015**, *370*, 20130263. [CrossRef]
22. Berger, S.; Sinha, A.K.; Roitsch, T. Plant physiology meets phytopathology: Plant primary metabolism and plant–pathogen interactions. *J. Exp. Bot.* **2007**, *58*, 4019–4026. [CrossRef] [PubMed]
23. Gitelson, A.A.; Gritz, Y.; Merzlyak, M.N. Relationships between leaf chlorophyll content and spectral reflectance and algorithms for non-destructive chlorophyll assessment in higher plant leaves. *J. Plant Physiol.* **2003**, *160*, 271–282. [CrossRef]
24. Chen, L.-J.; Fei, C.-Y.; Xu, Z.-P.; Wu, G.; Lin, H.-H.; Xi, D.-H. Positive role of phytochromes in *Nicotiana tabacum* against Cucumber mosaic virus via a salicylic acid-dependent pathway. *Plant Pathol.* **2018**, *67*, 488–498. [CrossRef]
25. Roelfs, A.P.; Singh, R.P.; Saari, E.E.; Broers, L.H.M.; Dubin, H.J.; Van Ginkel, M.; Nagarajan, S.; Payne, T.; Hettel, G.P. *Rust Diseases of Wheat: Concepts and Methods of Disease Management*; CIMMYT: Texcoco, Mexico, 1992; 81p.
26. Chen, X.M. Epidemiology and control of stripe rust [*Puccinia striiformis* f. sp. *tritici*] on wheat. *Can. J. Plant Pathol.* **2005**, *27*, 314–337. [CrossRef]
27. Bolton, M.D. Primary metabolism and plant defense—Fuel for the fire. *Mol. Plant Microbe Interact.* **2009**, *22*, 487–497. [CrossRef]
28. Torres-Sánchez, J.; Peña, J.M.; de Castro, A.I.; López-Granados, F. Multi-temporal mapping of the vegetation fraction in early-season wheat fields using images from UAV. *Comput. Electron. Agric.* **2014**, *103*, 104–113. [CrossRef]

29. Bendig, J.; Yu, K.; Aasen, H.; Bolten, A.; Bennertz, S.; Broscheit, J.; Gnyp, M.L.; Bareth, G. Combining UAV-based plant height from crop surface models, visible, and near infrared vegetation indices for biomass monitoring in barley. *Int. J. Appl. Earth Obs. Geoinf.* **2015**, *39*, 79–87. [CrossRef]
30. Vasseur, D.A.; Amarasekare, P.; Rudolf, V.H.; Levine, J.M. Eco-Evolutionary dynamics enable coexistence via neighbor-dependent selection. *Am. Nat.* **2011**, *178*, E96–E109. [CrossRef]
31. EL Jarroudi, M.; Kouadio, L.; Beyer, M.; Junk, J.; Hoffmann, L.; Tychon, B.; Maraite, H.; Bock, C.H.; Delfosse, P. Economics of a decision–support system for managing the main fungal diseases of winter wheat in the Grand-Duchy of Luxembourg. *Field Crops Res.* **2015**, *172*, 32–41. [CrossRef]
32. Zadoks, J.C.; Chang, T.T.; Konzak, C.F. A decimal code for the growth stages of cereals. *Weed Res.* **1974**, *14*, 415–421. [CrossRef]
33. Hou, Y.-C. Visual cryptography for color images. *Pattern Recognit.* **2003**, *36*, 1619–1629. [CrossRef]
34. Heidarian Dehkordi, R.; Denis, A.; Fouche, J.; Burgeon, V.; Cornelis, J.T.; Tychon, B.; Placencia Gomez, E.; Meersmans, J. Remotely-sensed assessment of the impact of century-old biochar on chicory crop growth using high-resolution UAV-based imagery. *Int. J. Appl. Earth. Obs. Geoinf.* **2020**, *91*, 102147. [CrossRef]
35. Dakos, V.; Carpenter, S.R.; Brock, W.A.; Ellison, A.M.; Guttal, V.; Ives, A.R.; Kéfi, S.; Livina, V.; Seekell, D.A.; van Nes, E.H.; et al. Methods for detecting early warnings of critical transitions in time series illustrated using simulated ecological data. *PLoS ONE* **2012**, *7*, e41010. [CrossRef]
36. R Core Team. *R: A Language and Environment for Statistical Computing*; R Foundation for Statistical Computing: Vienna, Austria, 2024. Available online: http://www.R-project.org/ (accessed on 10 July 2024).
37. Posit Team. *RStudio: Integrated Development Environment for R; Posit Software*; PBC: Boston, MA, USA, 2026. Available online: http://www.posit.co/ (accessed on 30 March 2026).
38. Jeger, M.; Van den Bosch, F. Threshold criteria for model plant disease epidemics. I. Asymptotic results. *Phytopathology* **1994**, *84*, 24–27. [CrossRef]
39. Madden, L.V.; Hughes, G. Plant disease incidence: Distributions, heterogeneity, and temporal analysis. *Annu. Rev. Phytopathol.* **1995**, *33*, 529–564. [CrossRef]
40. Segarra, J.; Jeger, M.J.; Van den Bosch, F. Epidemic dynamics and patterns of plant diseases. *Phytopathology* **2001**, *91*, 1001–1010. [CrossRef]
41. Gilligan, C.A. Sustainable agriculture and plant diseases: An epidemiological perspective. *Philos. Trans. R. Soc. Lond. Ser. B* **2007**, *363*, 741–759. [CrossRef] [PubMed]
42. Robert, C.; Bancal, M.-O.; Ney, B.; Lannou, C. Wheat leaf photosynthesis loss due to leaf rust, with respect to lesion development and leaf nitrogen status. *New Phytol.* **2005**, *165*, 227–241. [CrossRef]
43. Rossi, V.; Caffi, T.; Giosuè, S.; Bugiani, R. A mechanistic model simulating primary infections of downy mildew in grapevine. *Ecol. Modell.* **2008**, *212*, 480–491. [CrossRef]
44. Bock, C.H.; Chiang, K.-S.; Del Ponte, E.M. Plant disease severity estimated visually: A century of research, best practices, and opportunities for improving methods and practices to maximize accuracy. *Trop. Plant Pathol.* **2022**, *47*, 25–42. [CrossRef]
45. Morrison, L.W. Observer error in vegetation surveys: A review. *J. Plant Ecol.* **2016**, *9*, 367–379. [CrossRef]

Disclaimer/Publisher's Note: The statements, opinions and data contained in all publications are solely those of the individual author(s) and contributor(s) and not of MDPI and/or the editor(s). MDPI and/or the editor(s) disclaim responsibility for any injury to people or property resulting from any ideas, methods, instructions or products referred to in the content.